

# CFPNet-M: A Light-Weight Encoder-Decoder Based Network for Multimodal Biomedical Image Real-Time Segmentation

Ange Lou, Shuyue Guan and Murray Loew

**Abstract** — Currently, developments of deep learning techniques are providing instrumental to identify, classify, and quantify patterns in medical images. Segmentation is one of important applications in medical image analysis. In this regard, U-Net is the predominant approach to medical image segmentation tasks. However, we found that those U-Net based models have limitations in several aspects, for example, millions of parameters in the U-Net consuming considerable computation resource and memory, lack of global information, and missing some tough objects. Therefore, we applied two modifications to improve the U-Net model: 1) designed and added the dilated channel-wise CNN module, 2) simplified the U shape network. Based on these two modifications, we proposed a novel light-wight architecture – Channel-wise Feature Pyramid Network for Medicine (CFPNet-M). To evaluate our method, we selected five datasets with different modalities: thermography, electron microscopy, endoscopy, dermoscopy, and digital retinal images. And we compared its performance with several models having different parameter scales. This paper also involves our previous studies of DC-UNet and some commonly used light-weight neural networks. We applied the Tanimoto similarity instead of the Jaccard index for gray level image measurements. By comparison, CFPNet-M achieves a comparable segmentation results on all five medical datasets with only 0.65 million parameters, which is about 2% of U-Net, and 8.8 MB memory. Meanwhile, the inference speed can reach 80 FPS on a single RTX 2070Ti GPU with the  $256 \times 192$  pixels input size.

**Keywords** – real-time segmentation; medical image segmentation; light-weight segmentation model; dilated convolution; U-Net; CFPNet-M; Tanimoto similarity.

## 1. Introduction

The goals of medical image analysis are to provide efficient diagnostic and treatment process for the radiologists and clinicians [1]. Medical imaging devices such as X-ray, CT, and MRI can provide anatomic information of diseases and abnormality inside human body nondestructively. Since large amount of data and noises interference in medical images, it is important to process images and extract effective information [2] from them. The image processing technologies have many contributions in medical applications; for example, image segmentation, image registration and image-guided surgery are widely used in medical treatment.

In recent years, medical imaging has undergone tremendous developments in high-performing segmentation methods based on deep learning. Early segmentation models are mainly of encoder-decoder based neural networks like FCN [3], UNet [4], and SegNet [5]; they are widely used for segmentation in many scenes. Then, residual connection [6] has been applied to those encoder-decoder based model to help training and improve the efficiency of networks [7]. To solve the class imbalance problem (small organs or tumors) [8] in segmentation tasks without adding more training parameters, the Inception module [9] and dilated convolution [10] are introduced to design neural networks. For example, MutliResUNet [11] and DC-UNet [12] apply the simplified Inception module in UNet and successfully improve the performance for small tumor segmentations. To segment objects in different sizes, some networks like LEDNet [13] and ESPNet [14] introduce the dilated convolution to extract global feature information.

Even though applying those new convolutional techniques to improve segmentation performance, many state-of-art networks like Inception v3 [15], DeepLab [16] and MobileNet v2 [17] contain millions or tens of millions of parameters so that consume a large amount of computational resource and memory for training and prediction. In the field of semantic segmentations for autonomous driving, there have already been many light-wight networks with very good performances like ESPNetv2 [18], DABNet [19], and ICNet [20]; the mean Intersection over Union (mIoU) of their results can achieve 70% on Cityscapes [21] dataset. Recently, real-time segmentation plays a more and more important role in image-guided surgery [22] and medical robots [23] areas with the development of deep learning techniques. For the robotic surgery system, an effective and real-time image analysis is important to avoid the damages of surgical instruments on organs and tissues. However, there are limited studies about real-time segmentation networks in medical image segmentation area. In addition, each medical dataset has its specific challenges due to different imaging methods. Therefore, it is important to build a light-weight real-time segmentation network, which is compatible with various medical datasets.

In this study, in parallel to appreciating the capabilities of those encoder-decoder based models, we have discovered some techniques to improve segmentation performances and decrease the number of

parameters of models. Thus, we developed a novel model called Channel-wise Feature Pyramid Network for Medicine (CFPNet-M) from our previous work [24]. We tested the performance of our method on five different modalities biomedical datasets and compared the accuracy with other networks. Experiment results show that CFPNet-M has competitive accuracy and remarkable fewer parameters.

The contributions of this paper can be summarized as follow:

- We apply the dilated convolution and simplify the Inception module to design CFP module.
- Based on CFP module, we propose the CFPNet-M, which is a light-wight network for real-time medical image segmentations.
- We experiment with different biomedical datasets of different modalities, and CFPNet-M shows competitive accuracy and the superiority in terms of the parameter size and prediction speed.
- We examine both region (tumors and polyps) based and slim (neural structures and vessels) objects to show the ability of CFPNet-M for complex medical images.
- We introduce the Tanimoto similarity as measurement metric and compare its stability with other metrics.

## 2. Related Work

Recently, many deep learning-based methods have been proposed for the image segmentation. Compared with traditional methods, such as texture analysis and shape detection, deep learning-based methods are more automatic, accurate, and adaptive to objects segmentation in complicated situations, which are common to medical images. Thus, neural network models are ideal methods to apply for semantic segmentation of medical images.

### A. Encoder-Decoder-Based CNNs for Semantic Segmentation

The encoder-decoder-based network can be divided into two parts: encoder and decoder. Usually, the encoder is sequence of convolutional kernels and down-sampling operators used to extract high dimensional features. These features are supposed to contain the pixel-wise semantic information about the objects, edges, and background. And then, these features are decoded by up-sampling or deconvolutional operators to generate segmentation masks. Usually, the masks show the probabilities of pixels belonging to foreground or background. There are many encoder-decoder-based state-of-the-art implementations including FCN, SegNet and UNet. Especially, the UNet shows great potential in pixel-level medical image segmentation by achieving the best performances than others. In addition, the MutliResUNet [11] adds the Residual Paths from ResNet [6] to prevent a deeper network (depth increasing, i.e., more hidden layers) from gradient vanishing during training.

### B. Inception Module

The Inception module [9] proposed a parallel structure which contains  $1 \times 1$ ,  $3 \times 3$  and  $5 \times 5$  convolution kernel to obtain multi-scale feature maps (Figure 1a). Those large kernels, however, lead to great computational cost. Therefore, the feature version of the Inception module introduced the factorization to reduce the parameters and computational cost. The factorization operations contain two parts: factorization into smaller convolution kernel and asymmetric convolutions [15]. These two factorization methods have been applied widely in many networks (e.g., ResNext [25], Xception [26], and MobileNets [27]). The parallel structures in the Inception module increase the width of networks and provide multi-scale features (Figure 1c), and applying the factorization reduces the computational costs of becoming greater width. To provide more different-scale (more effective) features for segmentation, we propose the Channel-wise Feature Pyramid (CFP) module, which will be further discussed in the Method section.

### C. Dilated Convolution

Dilated convolution [28] introduced a special form of standard  $3 \times 3$  convolution by inserting gaps between pairs of convolution elements to enlarge the effective receptive field without introducing more parameters. The effective size of an  $n \times n$  dilated convolution kernel with a dilation rate  $r$  can be represented as:  $[r(n-1) + 1]^2$ . The dilation rate is the number of pixel gaps between adjacent convolution elements, and only  $n^2$  parameters participate in model training. In semantic segmentation area, many studies like ESPNetv2 [18], DABNet [19] and LEDNet [13] have used the dilated convolution kernels in their models and shown its advantage in pixel-level segmentation. The dilated convolution has

been shown the ability to extract large-scale features while maintaining the total number of parameters [51, 52]. Based on the considerations above, in this study, we apply the dilated convolution in every channel of the CFP module to further decrease parameters and make the model light-weight.

Designing the architectures of models is always a core study in deep learning. Some architectures like the ResNet [6] go deeper to extract higher-level features and some architectures like the InceptionNet [9] do wider to acquire more various features in the same level. In general, it is difficult to show that, for the deeper and wider networks, which one is the better architecture in deep learning. But for segmentation tasks, we consider choosing a wider architecture because it could provide multi-scale and different features from input images to form the final segmentation masks [15]. Unlike to classification or recognition tasks, image segmentations may not need very high-level features of objects. We think semantic segmentations may require more optional features to decide the boundaries and backgrounds. Thus, we introduce the CFP module for segmentations.

In segmentation applications, most current models are far from running in real-time ( $\geq 25$  FPS) [45]. For some applications like the autonomous driving, the characteristic of real-time is as important as accuracy. And real-time [48-50] and light-weight [46, 47] models are also required by medical segmentations used in some cases, for example, the real-time surgery assistant system and small/portable diagnosis devices. Recently, many deep learning segmentation models have been proposed; however, few of them well balance the speed, model size, and performance. Therefore, our CFP module aims to have a better balance among these aspects; especially, for applications of medical segmentations.

## 2. Method

In this section, we firstly introduce the basic element of the CNN module — the Channel-wise Feature Pyramid (CFP) module. Then, we present the structure of the CFP module and architecture of CFPNet-M.

### A. Feature Pyramid Channel

CFP module is based on the Feature Pyramid (FP) channel, a factorized form of convolution operator that decomposes a large kernel into a series of smaller convolution operator as shown in Figures 1(a) and (b). The Inception-v2 applied two  $3 \times 3$  convolutional operators to replace the  $5 \times 5$  kernel in the naïve version. Based on the idea of multi-scale feature maps, we design a module contains  $3 \times 3$ ,  $5 \times 5$ , and  $7 \times 7$  kernels as shown in Figures 1(c). Similar to Inception-v2, we applied a series of  $3 \times 3$  convolutional operators to replace  $5 \times 5$  and  $7 \times 7$  operators. Although this operation saves 28% and 45% of the parameters respectively, it still too many to achieve the goal of a light-weight model. Then, we applied the technique of MultiRes block [11] and merged those convolution kernels into one channel that contains only three  $3 \times 3$  operators. Moreover, we used the skip connection layer to concatenate features that are extracted from each convolutional operator to build our FP channel, as shown in Figure 1(d). Compared with Inception-v2-like implementation, the FP channel uses 50% fewer parameters but also retains the similar ability to learn multi-scale feature information.

Because of the concatenating features of each convolutional operator, to keep the same dimension of input and output, we rearranged filter numbers for each operator. For example, if the input dimension is  $N$ , we assigned  $N/4$  for the first and second operators, which correspond to the  $3 \times 3$  and  $5 \times 5$  convolutions, respectively. For the third block, which is the  $7 \times 7$  operator, we assigned  $N/2$  filters to extract large weighted sizeable features.

### B. CFP Module

The CFP module contains  $K$  FP channels with different dilation rates  $\{r_1, r_2, \dots, r_K\}$ . The original CFP module first applied a  $1 \times 1$  convolution to reduce the input dimension from  $M$  to  $M/K$ . Then, the dimension of the first to third operators are  $M/4K$ ,  $M/4K$ , and  $M/2K$ , respectively.

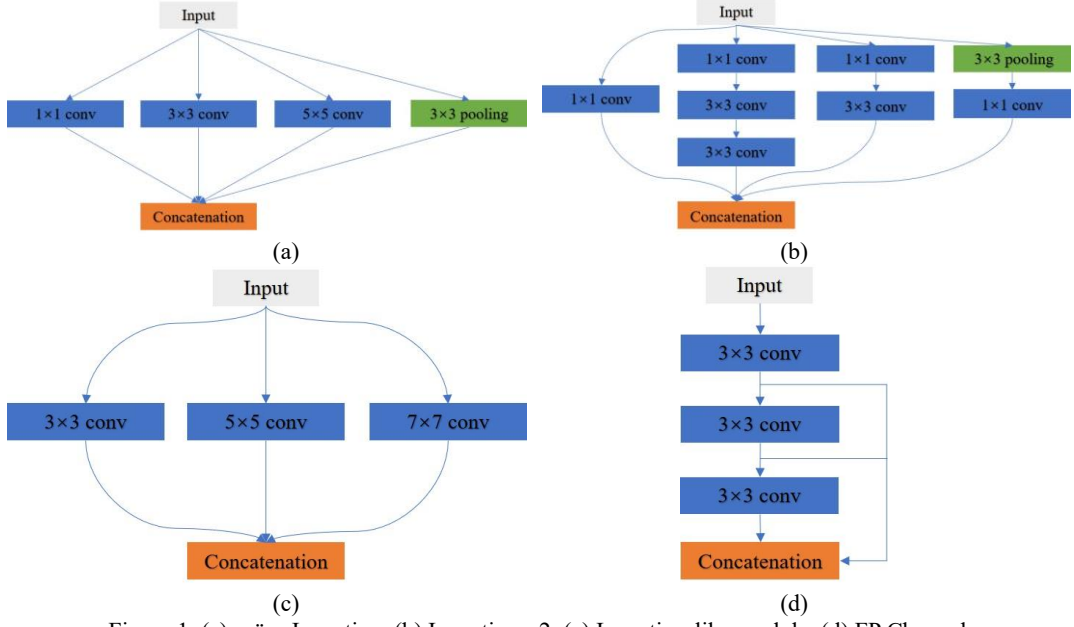


Figure 1. (a) naïve Inception, (b) Inception-v2, (c) Inception-like module, (d) FP Channel,

In Figure 2, we show more details about the CFP module. We use  $1 \times 1$  convolution to project high-dimension feature maps to low-dimension. Then, we set  $K$  FP channels into a parallel structure with different dilation rates. We then concatenate all feature maps into the input's dimension and use another  $1 \times 1$  convolution to activate the output. This is a basic structure of the original CFP module, as shown in Figure 2(a). Factorization increases the depth of the network, however, it causes the difficulty of training. Moreover, a simple fusion method leads to some unwanted checkerboard or gridding textures that greatly influence the accuracy and quality of segmentation [14]. Thus, we also introduced the Hierarchical Feature Fusion (HFF) [14] to eliminate those interferences. To solve the difficulty of training, we firstly used the residual connection to make a trainable deeper network and then to provide additional feature information [6]. Therefore, the final version of the CFP module is shown in Figure 2(b).

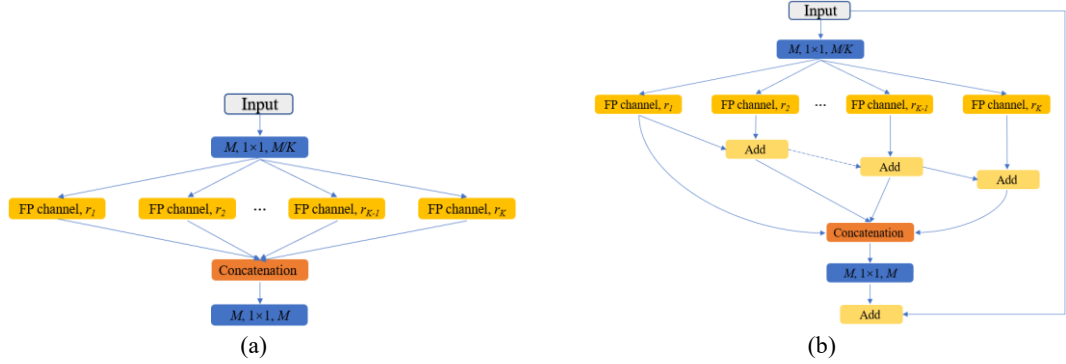


Figure 2. (a) Original CFP module. (b) CFP module

### C. CFPNet-M

**Setup CFP module:** First, we specify the details about the CFP module (Figure 2b) which we used to build the CFPNet-M. We choose the number of FP channels  $K = 4$ . For the input with dimension like  $M = 32$ , the total filter number of each channel is 8. And we set the filter numbers of the first to third convolutional operators are 2, 2 and 4, respectively. Then, we set different dilation rates for each FP channel. The dilation rate is equal to  $r_K$ ; for example, we set the first and forth channels' dilation rate is  $r_1 = 1$  and  $r_K$ . To extract local and global features, we set dilation rates of second and third channels are  $r_2 = r_K/4$  and  $r_3 = r_K/2$ , respectively. Therefore, the CFP module could learn those medium-size features. Note: if  $r_K/4 < 1$ , e.g.,  $r_K = 2$ , we directly set this channel's dilation rate as 1.

Table 1. Architecture details of CFPNet-M.

No.	Layer	Mode	Dimension
1	$3 \times 3$ Conv	Stride 2	32
2	$3 \times 3$ Conv	Stride 1	32
3	$3 \times 3$ Conv	Stride 1	32
4	Ave pooling	-	-
5-6	$2 \times \text{CFP}$	$r_K = 2$	64
7	Ave pooling	-	-
8-9	$2 \times \text{CFP}$	$r_K = 4$	128
10-11	$2 \times \text{CFP}$	$r_K = 8$	128
12-13	$2 \times \text{CFP}$	$r_K = 16$	128
14	Deconv	Stride 2	128
15	Deconv	Stride 2	64
16	Deconv	Stride 2	32
17	$1 \times 1$ Conv	Stride 1	1

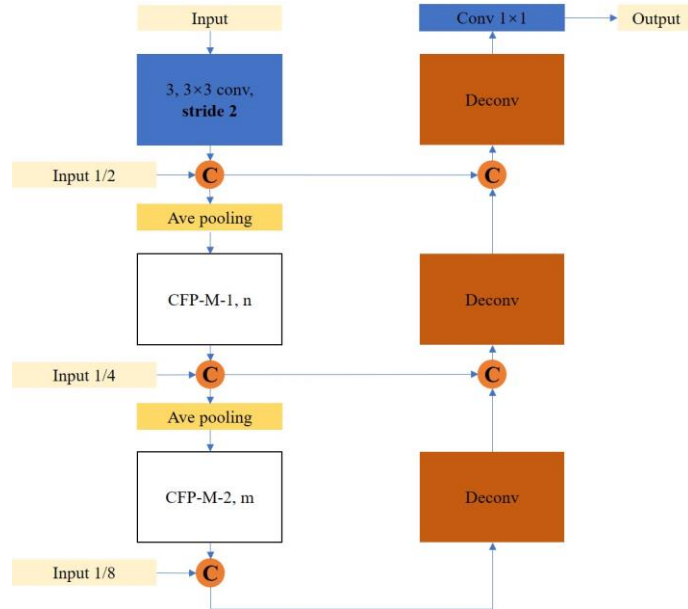


Figure 3. Architecture of CFPNet-M

**Network architecture:** Since our goal is to build a light-weight network but have competitive performance, we build a shallow U-shape network as shown in Figure 3. And the details of the architecture are in Table 1. We firstly use three  $3 \times 3$  convolutional operators as the initial feature extractor. The first operators with stride 2 to apply down-sampling. After initial extractor, we applied the average pooling for down-sampling. Then, we insert the first CFP module clusters (CFP-M-1), repeating  $n$  times. Before the second CFP module clusters (CFP-M-2), we also insert an average pooling layer to down-sample the feature maps. We repeat the CFP modules  $m$  times to build the CFP-M-2 cluster. Before the decoder, we inject resized input images to provide additional feature information for the segmentation network. Then, we apply three deconvolutional operators with stride 2 to build the decoder and connect the same stage encoders by skip connections. Finally, we use a  $1 \times 1$  convolution to activate the final feature map and generate segmentation masks. In the CFPNet-M, we choose the repeat times of CFP module  $n = 2$  and  $m = 6$  with the dilation rate  $r_{K_{CFP-M-1}} = [2,2]$  and  $r_{K_{CFP-M-2}} = [4,4,8,8,16,16]$ .

### 3. Experiments

In this section, we test our purposed segmentation neural network - CFPNet-M on five datasets: our own infrared breast dataset and the ISBI-2012 (Electron Microscopy), ISIC-2018 (Dermoscopy), CVC-ClinicDB (Endoscopy), and DRIVE (Digital Retinal Images); these datasets are widely used to estimate medical segmentation methods.

#### A. Datasets

**Our Breast Thermography Images.** We collected breast infrared images by using the N2 Imager (N2 Imaging System, Irvine, Calif.). Our breast dataset contains 450 infrared images from 14 patients and 16 healthy volunteers; all images have been removed the background and denoised. Each participant was imaged for a total time of 15 minutes, capturing one image every minute (15 images per participant). The original sizes of images range from  $540 \times 260$  to  $610 \times 290$  (pixels); we have uniformly resized them to  $256 \times 128$  before training.

**Electron Microscopy Images.** To show the performance of CFPNet-M on electron microscopy images, we used the dataset of the ISBI-2012; 2D EM segmentation challenge [29, 30]. This dataset contains 30 images in training set from a serial section Transmission Electron Microscopy (ssTEM) of the Drosophila first instar larva ventral nerve cord [30]. We chose those 30 images as dataset, and resized resolution from  $512 \times 512$  to  $256 \times 256$ .

**Endoscopy Images.** We used CVC-ClinicDB [31] to show the performance of CFPNet-M in endoscopy images. Those images were extracted from the colonoscopy videos. The dataset contains total 612 images with original size  $384 \times 288$ . We resized them to  $256 \times 192$  for training.

**Dermoscopy Images.** We acquired the Dermoscopy images from the ISIC-2018: Lesion Boundary Segmentation challenge dataset. The data for ISIC-2018 were from the ISIC-2017 [32] and the HAM10000 dataset [33]. The compiled dataset contains a total of 2594 images of different types of skin lesions with expert annotations. Before training, we resized those images to  $256 \times 192$ .

**Digital Retinal Images.** We applied DRIVE [34] to test the performance of CFPNet-M on slim objects. This dataset was established to help study cardiovascular and ophthalmologic diseases such as diabetes, hypertension, and arteriosclerosis. We used 20 RGB images from its training set and resized them from  $512 \times 512$  to  $256 \times 256$ .

The summarized details of these five datasets can be found in Table 2.

Table 2. Overview of datasets.

Modality	Dataset	No. of images	Original resolution	Input resolution
Thermography	IR breast	450	Variable	$256 \times 128$
Electron microscopy	ISBI-2012	30	$512 \times 512$	$256 \times 256$
Endoscopy	CVC-Clinic DB	612	$384 \times 288$	$256 \times 192$
Dermoscopy	ISCI-2018	2594	Variable	$256 \times 192$
Digital Retinal	DRIVE	20	$512 \times 512$	$256 \times 256$

### B. Cross-validation

Cross-Validation is widely used to test models' performance. In the  $k$ -fold cross-validation test, the dataset  $D$  is randomly split into  $k$  mutually exclusive subsets  $D_1, D_2, \dots, D_k$  of approximately equal size [35]. The model is tested  $k$  times; for each time, one of the  $k$  subsets is chosen as the validation set and other  $k - 1$  subsets as the training set. We estimated the performance of model via overall results of  $k$  times training. For our own infrared breast dataset, we select  $k = 30$  because of 30 individual participants. And we choose  $k = 5$  for other four public datasets.

### C. Measurement metric

To evaluate the performance of segmentation, we need a method to compare the segmented region with ground truth. Since we applied the Sigmoid function to activate the final convolutional operator, the output is a gray level image which maps in range  $[0, 1]$ . Therefore, we need to do thresholding before calculating accuracy. Usually, thresholding grayscale image to binary (binarization) [36] introduces additional errors. Currently, there are lots of popular comparison methods between two images:

- Binary to binary: Jaccard Similarity (JS) [37]
- Gray to gray: Mean Absolute Error (MAE) [38]; Tanimoto Similarity [39] (extended Jaccard Similarity); Structural Similarity (SSIM) [40].

In our previous studies, we chose JS as measurement metric; to consider two binary images as two sets  $A$  and  $B$ , their JS value is:

$$JS(A, B) = \frac{|A \cap B|}{|A \cup B|} \quad (1)$$

Before comparison, we did thresholding by using Otsu [41] algorithm. The workflow is shown in the Figure 4.

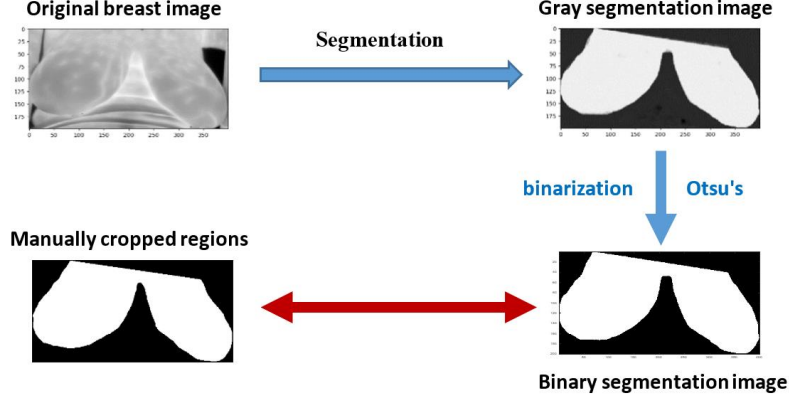


Figure 4. Workflow of Jaccard similarity.

Since Otsu lead some thresholding errors, we turn to consider some gray-to-gray comparison methods. One of simply and widely used method is the Mean Absolute Error (MAE). In general, for two images (same size)  $A$  and  $B$ , their MAE value is:

$$MAE(A, B) = 1 - \frac{|A - B|}{maxE} \quad (2)$$

The **maxE** is maximum error value, to 8-bit gray-scale images (size:  $W \times L$ ),  $maxE = W \times L \times 2^8$ .

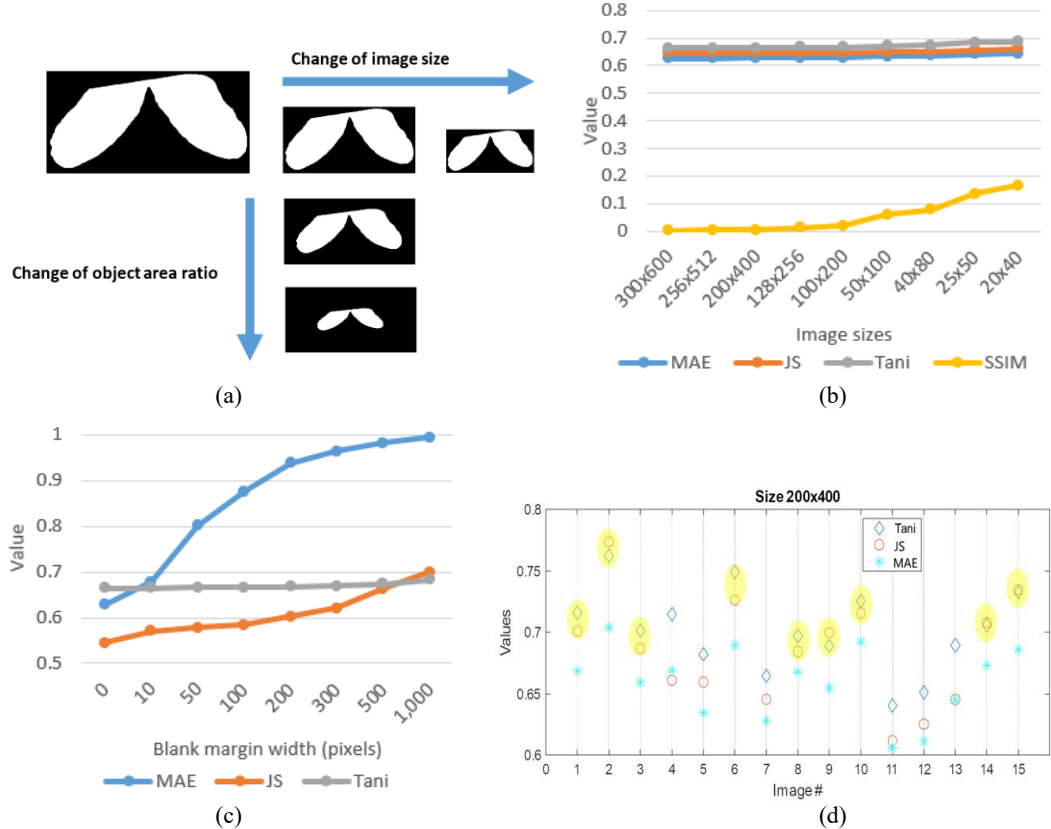


Figure 5. (a) size and ratio change of images. (b) accuracy value vs image size. (c) accuracy vs object ratio. (d) comparison of three measurement metrics

The Tanimoto similarity, also called extended JS, can be considered as a grayscale JS. For binary image, JS compares images by union and intersection operations. The union operation could be considered as sum of products. For two set  $A$  and  $B$ :

$$|A \cap B| = \sum a_i b_i \quad (3)$$

Where  $a_i \in A, b_i \in B$ . This equation holds if  $a_i, b_i \in \{0, 1\}$ , which are binary values. But if  $a_i, b_i$  are not binary, we use sum of products (right part) instead of the union operation. Since:

$$|A \cap B| = \sum a_i^2 \quad (4)$$

And,

$$|A \cup B| = |A| + |B| - |A \cap B| = \sum (a_i^2 + b_i^2 - a_i b_i) \quad (5)$$

For gray-gray comparison, according to  $JS(A, B)$ , the value of Tanimoto similarity is:

$$T(A, B) = \frac{\sum a_i b_i}{\sum (a_i^2 + b_i^2 - a_i b_i)} \quad (6)$$

To prove the Tanimoto similarity is an ideal measurement metric, we tested different measurement metrics on different sizes and object areas ratio images as show in Figure 5(a). Each result is the average value of all (15) samples of one case from our infrared breast dataset. For each sample, the value is calculated by comparing ground truth image with C-DCNN segmented image [41]. From Figure 5(b) and (c), the results show that SSIM is not stable to image size changing and only the Tanimoto similarity keeps stable to changes of object area ratio.

Furthermore, Figure 5(d) shows comparison results by Tanimoto similarity, JS and MAE for the 15 samples in size  $400 \times 200$ . Results indicate that for majority samples (9/15, yellow mark), Tanimoto similarity values are close to JS. Therefore, Tanimoto similarity is a good alternative measure instead of JS for grayscale image comparisons. Based on our analysis, we choose Tanimoto similarity instead of Jaccard as measurement metric in our experiments.

Table 3. Details of network in experiments. Note: U-Net\* is original U-Net architecture, the U-Net we used in experiments is doubled filter numbers [12]. The model file size is measure with specific input size  $256 \times 128$ .

Model	Parameters	Model file size (MB)	Mean Tanimoto (%)	Std
U-Net*	7,750,821	88.8	88.70	0.0256
U-Net	31,031,685	354.0	89.80	0.0241
Inception v3	29,896,689	343.0	<b>93.17</b>	0.0279
MultiResUNet	29,061,741	333.0	91.50	0.0237
EfficientNet-b0	10,071,501	116.0	92.70	0.0272
DC-UNet	10,069,640	116.0	92.70	0.0215
MobileNet v2	8,011,345	92.5	92.25	0.0278
ICNet	6,740,481	77.7	84.80	0.0458
ESPNet	579,961	7.3	89.70	0.0250
ENet	365,638	5.1	82.90	0.0479
CFPNet-M	654,279	8.8	92.20	0.0211

Table 4. Results of EM datasets (ISBI-2012).

Model	Fold 1	Fold 2	Fold 3	Fold 4	Fold 5	Mean Tanimoto (%)	Std
U-Net	90.75	89.31	91.33	92.65	91.60	91.13	0.0157
Inception v3	89.51	88.51	89.40	88.16	87.56	88.63	0.0074
MultiResUNet	90.83	91.16	92.64	93.11	92.08	91.96	0.0121
EfficientNet-b0	88.63	89.07	87.55	88.73	88.43	88.48	0.0051
DC-UNet	91.79	91.27	93.21	93.44	93.38	<b>92.62</b>	0.0092
MobileNet v2	89.06	88.97	88.93	89.23	89.12	89.06	0.0011
ICNet	69.00	66.51	71.20	71.92	69.71	69.67	0.0189
ESPNet	80.64	82.55	86.31	85.91	86.04	84.29	0.0179
ENet	64.02	72.63	66.14	64.78	69.13	67.34	0.0276
CFPNet-M	90.42	90.42	92.57	91.39	92.42	91.44	0.0111

Table 5. Results of endoscopy datasets (CVC-ClinicDB).

Model	Fold 1	Fold 2	Fold 3	Fold 4	Fold 5	Mean Tanimoto (%)	Std
U-Net	74.03	70.81	67.96	63.26	71.52	69.52	0.0368
Inception v3	86.28	86.95	83.26	81.51	83.43	84.29	0.0203
MultiResUNet	81.82	80.34	79.57	74.23	78.66	78.92	0.0257
EfficientNet-b0	87.32	87.31	85.72	84.39	85.64	<b>86.08</b>	0.0112
DC-UNet	83.11	82.51	81.10	78.60	80.19	80.94	0.0162
MobileNet v2	84.44	85.50	83.02	81.03	82.28	83.25	0.0158
ICNet	71.00	72.60	69.52	61.28	68.60	68.60	0.0390
ESPNet	55.55	59.57	56.30	54.77	58.48	56.94	0.0181
ENet	77.14	73.17	63.58	66.10	70.35	70.01	0.0485
CFPNet-M	80.31	81.86	78.09	75.43	78.49	78.84	0.0217

Table 6. Results of Dermoscopy datasets (ISIC-2018).

Model	Fold 1	Fold 2	Fold 3	Fold 4	Fold 5	Mean Tanimoto (%)	Std
U-Net	79.68	79.93	80.40	80.64	76.73	79.48	0.0141
Inception v3	82.36	82.32	82.63	83.54	82.74	82.70	0.0041
MultiResUNet	80.75	80.23	80.51	81.54	80.12	80.63	0.0051
EfficientNet-b0	83.06	83.28	83.62	83.94	83.13	<b>83.41</b>	0.0033
DC-UNet	80.21	81.80	82.62	82.99	80.63	81.65	0.0108
MobileNet v2	81.38	82.21	82.19	82.70	81.92	82.08	0.0043
ICNet	78.02	78.48	76.89	80.80	78.08	78.45	0.0129
ESPNet	76.49	78.30	73.41	80.84	75.45	76.90	0.0253
ENet	79.01	80.29	79.95	79.78	79.77	79.76	0.0042
CFPNet-M	81.07	81.68	81.75	83.06	81.83	81.88	0.0065

Table 7. Results of digital retinal datasets (DRIVE).

Model	Fold 1	Fold 2	Fold 3	Fold 4	Fold 5	Mean Tanimoto (%)	Std
U-Net	55.35	46.80	57.87	58.66	52.05	54.15	0.0434
Inception v3	52.23	57.51	57.92	56.95	56.38	56.20	0.0205
MultiResUNet	59.31	58.41	59.40	60.12	56.28	58.70	0.0133
EfficientNet-b0	58.57	57.40	58.97	58.17	54.12	57.44	0.0174
DC-UNet	60.89	59.59	60.54	60.16	57.93	<b>59.82</b>	0.0104
MobileNet v2	53.87	57.86	59.56	56.74	57.72	57.15	0.0187
ICNet	44.22	47.63	40.16	45.97	41.67	43.93	0.0273
ESPNet	54.07	57.30	55.25	57.32	49.75	54.74	0.0279
ENet	55.97	56.95	53.22	56.46	52.00	54.92	0.0195
CFPNet-M	58.59	58.17	58.32	59.37	57.22	57.15	0.0069

Table 9. Speed and complexity of each model.

Model	Parameters	Model file size (MB)	Speed (FPS)	FLOPS
U-Net	31,031,685	354.0	50	464,925,202
Inception v3	29,896,689	343.0	33	358,813,094
MultiResUNet	29,061,741	333.0	21	108,715,188
EfficientNet-b0	10,071,501	116.0	54	120,862,094
DC-UNet	10,069,640	116.0	17	160,517,331
MobileNet v2	8,011,345	92.5	81	96,154,791
ICNet	6,740,481	77.7	130	565,733,942
ESPNet	579,961	7.3	129	8,668,267
ENet	365,638	5.1	168	5,370,508
CFPNet-M	654,279	8.8	80	9,740,456

#### D. Implementation protocol

CFPNet-M is trained by using Keras [42] with CUDA 9.0, cuDNN V7, and a single RTX 2070Ti GPU. For network training, we choose Adam as the optimizer with parameter  $\beta_1 = 0.9$  and  $\beta_2 = 0.999$ . We set initial learning rate 0.001 and apply the binary cross-entropy as loss function.

## 4. Results

In the experiments, we choose 10 neural networks with the number of parameters distributes at different levels (less than 1 million, millions, and tens of millions). The details of those networks are shown in Table 3. We test the performance of U-Net [4], Inception v3 [15], MultiResUNet [11], EfficientNet\_b0 [43], DC-UNet [12], MobileNet v2 [17], ICNet[20], ESPNet [14], ENet [44], and our CFPNet-M on five datasets; and then compare their results.

#### A. Segmentation results

The IR breast dataset contains images from 30 persons; we divide them into 30 subsets (one subset for one person) for 30-fold cross-validation. The Tanimoto accuracy of each subset is shown in Table 8, in Appendix. We report the mean Tanimoto similarity and standard deviation (Std) of those networks at Table 3. The best mean Tanimoto shows in bold font.

For the four public medical datasets, we randomly divide them into 5 folds and calculate mean Tanimoto similarity and Std. The results are shown in Table 4 to 7. In all experiments, we do not apply additional data augmentation and enhancement techniques. And for the DRIVE dataset, we do not take any post-processing (e.g., extract objects from field of view). We also display some segmentation results of thin objects in the Figure 6 and Figure 7. And the segmentation results of region-based objects are shown in Figure 8 to 10.

#### B. Inference speeds and complexity comparison

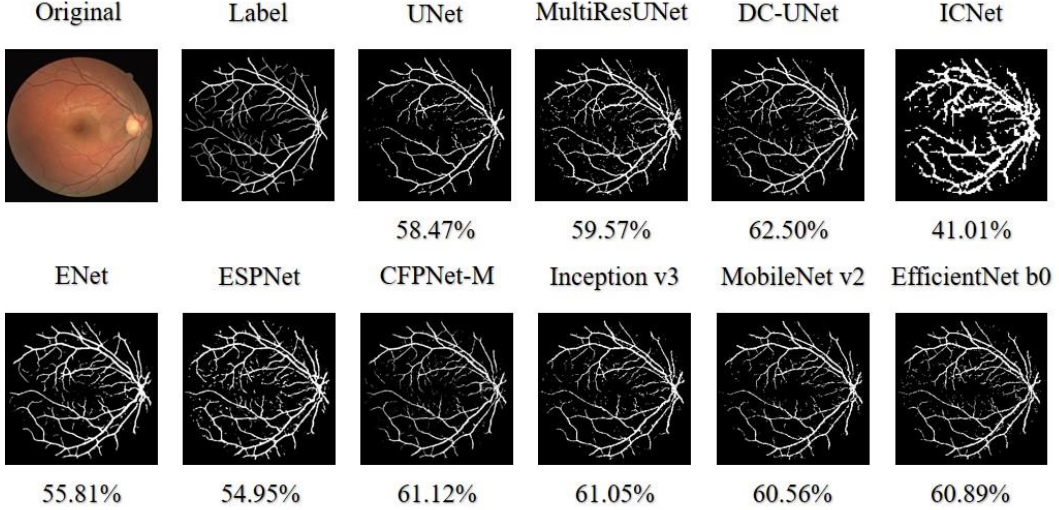


Figure 6. Segmentation of DRIVE.

Inference speed evaluation is performed on a single RTX 2070Ti GPU, we report an average of 500 frames of CVC-ClinicDB dataset for the Frames Per Second (FPS) measurement. To compare the complexity of models, we calculate the floating-point operations (FLOPs) of each network. We report the speeds and complexity of each network in Table 9.

## 5. Discussion

In these experiments, CFPNet-M shows great potential in both region based and thin object medical image segmentation among models whose numbers of parameters are fewer than 1 million (light-weight models). In our infrared breast dataset, as shown in Figure 8, only CFPNet-M can well separate the belly and breast region in light-weight models. According to the average accuracy of infrared breast dataset, the segmentation performance of CFPNet-M is competitive with those state-of-the-arts models in semantic segmentation, like the Inception v3. It is noteworthy that the number of parameters of CFPNet-M is only about 2.2%, 6.5% and, 8.2% of that of Inception v3, EfficientNet-b0, and MobileNet v2 models.

To thin objects datasets like ISBI-2012 (Table 4) and DRIVE (Table 7), the DC-UNet [12] model that proposed in our previous studies performs best. In fact, the CFPNet-M derives from the DC-UNet with much fewer parameters. The CFPNet-M has only about 6.5% parameters of the DC-UNet, but its mean accuracy is slightly smaller than the DC-UNet; and CFPNet-M also shows a good segmentation performance compared with other models we tested.

For ISIC-2018 dataset (region-based segmentation, Table 6), CFPNet-M shows competitive segmentation accuracy but using much fewer parameters. For example, CFPNet-M obtains the mean accuracy very close to the MobileNet v2 and from Table 9, its speed is also similar to the MobileNet v2. However, CFPNet-M has only about 8.2% parameters of the MobileNet v2. Another example is, on the CVC-ClinicDB dataset (Table 5), which contains many challenge cases with small objects, vague boundaries, and unbalanced illumination, although the Inception v3, MobileNet v2, and EfficientNet-b0 have better segmentation results than others, CFPNet-M still obtains competitive segmentation results on those non-challenge cases as shown in Figure 9.

The remarkable advantage of CFPNet-M is it has much fewer parameters than those state-of-the-arts models but retains competitively good segmentation performances. It makes the CFPNet-M a light-weight network and the real-time segmentation for multimodal biomedical images to become realizable. We used split-and-merge strategy to reduce the dimension of input and output to minimize the parameters of network. Moreover, we introduced the Hierarchical Feature Fusion (HFF) to eliminate the gridding textures to further improve the segmentation quality. Nevertheless, the multi-channel design enlarges the receptive field and builds a more effective feature pyramid for the encoder. To take a CFP-M module with the dilated rate = 16 as an example, the receptive field at the fourth channel can reach  $103 \times 103$  pixels, which is larger than  $33 \times 33$  in the ESPNet.

In addition, we report the size, speed, and complexity of each model in Table 9. CFPNet-M not only has fewer parameters and smaller network size but also has lower complexity and higher speeds compared with many state-of-the-art models. Competitive performance, high speed, small size, and low

network complexity makes CFPNet-M more suitable to be deployed on portable devices.

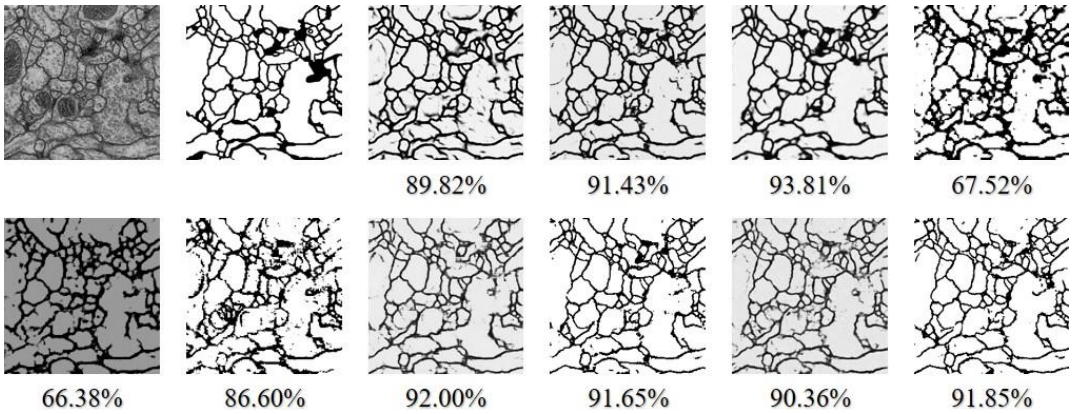


Figure 7. Segmentation of ISBI-2012.

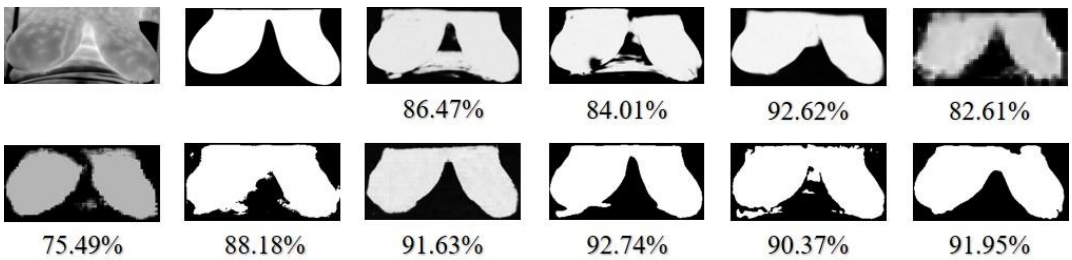


Figure 8. Segmentation of Infrared breast dataset.

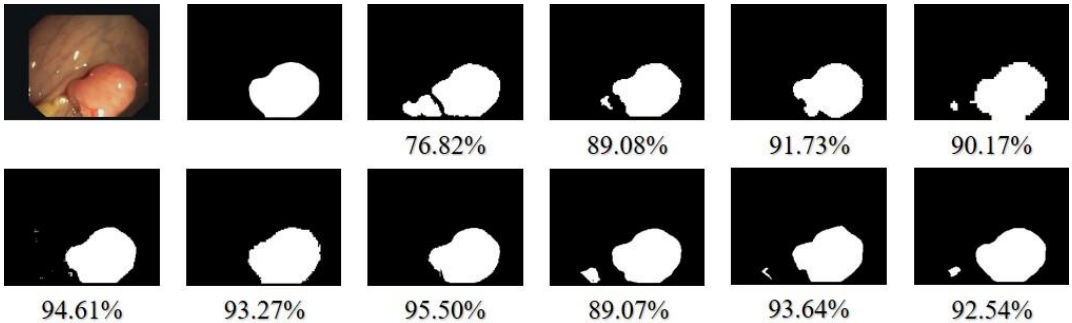


Figure 9. Segmentation of CVC-ClinicDB.

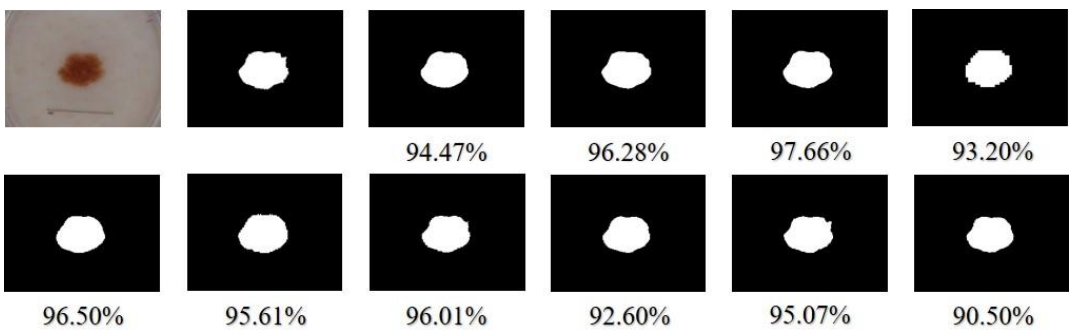


Figure 10. Segmentation of ISIC-2018.

## 6. Conclusion

In this paper, we analyzed the architecture of the proposed CFPNet-M and compared its performance with some state-of-the-art networks. We selected four public datasets and our own infrared breast dataset to test and compare the performances of ten models including the CFPNet-M for medical image segmentation. The CFPNet-M shows competitive performances and has great advantages of much fewer parameters and smaller model file size. In addition, we also tested its segmentation speeds -- it can reach

80 FPS with  $256 \times 192$  input size on a single RTX 2070Ti GPU. Its great real-time performance could help medical applications such as the image-guided surgery and vision based medical robots. Therefore, we believe that the CFPNet-M is a novel and promising light-weight network for real-time medical image segmentations.

## Reference

- [1] J. Gao, Q. Jiang, B. Zhou, and D. Chen, “Convolutional neural networks for computer-aided detection or diagnosis in medical image analysis: an overview,” *Math. Biosci. Eng.*, vol. 16, no. 6, pp. 6536–6561, 2019.
- [2] H. Song, A.-D. Nguyen, M. Gong, and S. Lee, “A review of computer vision methods for purpose on computer-aided diagnosis,” *Journal of International Society for Simulation Surgery*, vol. 3, no. 1, pp. 1–8, 2016.
- [3] Long, J., Shelhamer, E., & Darrell, T. (2015). Fully convolutional networks for semantic segmentation. In *Proceedings of the IEEE conference on computer vision and pattern recognition* (pp. 3431-3440).
- [4] Ronneberger, O., Fischer, P., & Brox, T. (2015, October). U-net: Convolutional networks for biomedical image segmentation. In *International Conference on Medical image computing and computer-assisted intervention* (pp. 234-241). Springer, Cham.
- [5] Badrinarayanan, V., Kendall, A., & Cipolla, R. (2017). Segnet: A deep convolutional encoder-decoder architecture for image segmentation. *IEEE transactions on pattern analysis and machine intelligence*, 39(12), 2481-2495.
- [6] He, K., Zhang, X., Ren, S., & Sun, J. (2016). Deep residual learning for image recognition. In *Proceedings of the IEEE conference on computer vision and pattern recognition* (pp. 770-778).
- [7] Zhang, Z., Liu, Q., & Wang, Y. (2018). Road extraction by deep residual u-net. *IEEE Geoscience and Remote Sensing Letters*, 15(5), 749-753.
- [8] Hesamian, M. H., Jia, W., He, X., & Kennedy, P. (2019). Deep learning techniques for medical image segmentation: achievements and challenges. *Journal of digital imaging*, 32(4), 582-596.
- [9] Szegedy, C., Liu, W., Jia, Y., Sermanet, P., Reed, S., Anguelov, D., ... & Rabinovich, A. (2015). Going deeper with convolutions. In *Proceedings of the IEEE conference on computer vision and pattern recognition* (pp. 1-9).
- [10] Wang, P., Chen, P., Yuan, Y., Liu, D., Huang, Z., Hou, X., & Cottrell, G. (2018, March). Understanding convolution for semantic segmentation. In *2018 IEEE winter conference on applications of computer vision (WACV)* (pp. 1451-1460). IEEE.
- [11] Ibtehaz, N., & Rahman, M. S. (2020). MultiResUNet: Rethinking the U-Net architecture for multimodal biomedical image segmentation. *Neural Networks*, 121, 74-87.
- [12] Lou, A., Guan, S., & Loew, M. H. (2021, February). DC-UNet: rethinking the U-Net architecture with dual channel efficient CNN for medical image segmentation. In *Medical Imaging 2021: Image Processing* (Vol. 11596, p. 115962T). International Society for Optics and Photonics.
- [13] Wang, Y., Zhou, Q., Liu, J., Xiong, J., Gao, G., Wu, X., & Latecki, L. J. (2019, September). Lednet: A lightweight encoder-decoder network for real-time semantic segmentation. In *2019 IEEE International Conference on Image Processing (ICIP)* (pp. 1860-1864). IEEE.
- [14] Mehta, S., Rastegari, M., Caspi, A., Shapiro, L., & Hajishirzi, H. (2018). Espnet: Efficient spatial pyramid of dilated convolutions for semantic segmentation. In *Proceedings of the european conference on computer vision (ECCV)* (pp. 552-568).
- [15] C. Szegedy, V. Vanhoucke, S. Ioffe, J. Shlens, and Z. Wojna, “Rethinking the inception architecture for computer vision,” in *Proceedings of the IEEE conference on computer vision and pattern recognition*, pp. 2818–2826, 2016.
- [16] Chen, L. C., Papandreou, G., Kokkinos, I., Murphy, K., & Yuille, A. L. (2017). Deeplab: Semantic image segmentation with deep convolutional nets, atrous convolution, and fully connected crfs. *IEEE transactions on pattern analysis and machine intelligence*, 40(4), 834-848.
- [17] Sandler, M., Howard, A., Zhu, M., Zhmoginov, A., & Chen, L. C. (2018). Mobilenetv2: Inverted residuals and linear bottlenecks. In *Proceedings of the IEEE conference on computer vision and pattern recognition* (pp. 4510-4520).
- [18] Mehta, S., Rastegari, M., Shapiro, L., & Hajishirzi, H. (2019). Espnetv2: A light-weight, power efficient, and general purpose convolutional neural network. In *Proceedings of the IEEE/CVF Conference on Computer Vision and Pattern Recognition* (pp. 9190-9200).
- [19] Li, G., Yun, I., Kim, J., & Kim, J. (2019). Dabnet: Depth-wise asymmetric bottleneck for real-time semantic segmentation. *arXiv preprint arXiv:1907.11357*.
- [20] Zhao, H., Qi, X., Shen, X., Shi, J., & Jia, J. (2018). Icnet for real-time semantic segmentation on high-resolution images. In *Proceedings of the European conference on computer vision (ECCV)* (pp. 405-420).
- [21] Cordts, M., Omran, M., Ramos, S., Rehfeld, T., Enzweiler, M., Benenson, R., ... & Schiele, B. (2016). The cityscapes dataset for semantic urban scene understanding. In *Proceedings of the IEEE conference on computer vision and pattern recognition* (pp. 3213-3223).
- [22] Choi, B., Jo, K., Choi, S., & Choi, J. (2017, July). Surgical-tools detection based on Convolutional Neural Network in laparoscopic robot-assisted surgery. In *2017 39th Annual International Conference of the IEEE Engineering in Medicine and Biology Society (EMBC)* (pp. 1756-1759). Ieee.
- [23] Liu, Y., Zhao, Z., Chang, F., & Hu, S. (2020). An anchor-free convolutional neural network for real-time surgical tool detection in robot-assisted surgery. *IEEE Access*, 8, 78193-78201.

[24] Lou, A., & Loew, M. (2021). CFPNet: Channel-wise Feature Pyramid for Real-Time Semantic Segmentation. arXiv preprint arXiv:2103.12212.

[25] Xie, S., Girshick, R., Dollár, P., Tu, Z., & He, K. (2017). Aggregated residual transformations for deep neural networks. In *Proceedings of the IEEE conference on computer vision and pattern recognition* (pp. 1492-1500).

[26] Chollet, F. (2017). Xception: Deep learning with depthwise separable convolutions. In *Proceedings of the IEEE conference on computer vision and pattern recognition* (pp. 1251-1258).

[27] A. G. Howard, M. Zhu, B. Chen, D. Kalenichenko, W. Wang, T. Weyand, M. Andreetto, and H. Adam, "Mobilenets: Efficient convolutional neural networks for mobile vision applications," arXiv preprint arXiv:1704.04861, 2017.

[28] M. Holschneider, R. Kronland-Martinet, J. Morlet, and P. Tchamitchian, "A realtime algorithm for signal analysis with the help of the wavelet transform," in *Wavelets*, pp. 286-297, Springer, 1990.

[29] Arganda-Carreras, I., Turaga, S. C., Berger, D. R., Cireşan, D., Giusti, A., Gambardella, L. M., ... & Seung, H. S. (2015). Crowdsourcing the creation of image segmentation algorithms for connectomics. *Frontiers in neuroanatomy*, 9, 142.

[30] Cardona, A., Saalfeld, S., Preibisch, S., Schmid, B., Cheng, A., Pulokas, J., ... & Hartenstein, V. (2010). An integrated micro-and macroarchitectural analysis of the Drosophila brain by computer-assisted serial section electron microscopy. *PLoS Biol*, 8(10), e1000502.

[31] Bernal, J., Sánchez, F. J., Fernández-Esparrach, G., Gil, D., Rodríguez, C., & Vilariño, F. (2015). WM-DOVA maps for accurate polyp highlighting in colonoscopy: Validation vs. saliency maps from physicians. *Computerized Medical Imaging and Graphics*, 43, 99-111.

[32] Codella, N. C., Gutman, D., Celebi, M. E., Helba, B., Marchetti, M. A., Dusza, S. W., ... & Halpern, A. (2018, April). Skin lesion analysis toward melanoma detection: A challenge at the 2017 international symposium on biomedical imaging (isbi), hosted by the international skin imaging collaboration (isic). In *2018 IEEE 15th International Symposium on Biomedical Imaging (ISBI 2018)* (pp. 168-172). IEEE.

[33] Tschandl, P., Rosendahl, C., & Kittler, H. (2018). The HAM10000 dataset, a large collection of multi-source dermatoscopic images of common pigmented skin lesions. *Scientific data*, 5(1), 1-9.

[34] Staal, J., Abràmoff, M. D., Niemeijer, M., Viergever, M. A., & Van Ginneken, B. (2004). Ridge-based vessel segmentation in color images of the retina. *IEEE transactions on medical imaging*, 23(4), 501-509.

[35] Kohavi, R. (1995, August). A study of cross-validation and bootstrap for accuracy estimation and model selection. In *Ijcai* (Vol. 14, No. 2, pp. 1137-1145).

[36] Sezgin, M., & Sankur, B. (2004). Survey over image thresholding techniques and quantitative performance evaluation. *Journal of Electronic Imaging*, 13(1), 146-165.

[37] Kosub, S. (2019). A note on the triangle inequality for the Jaccard distance. *Pattern Recognition Letters*, 120, 36-38.

[38] Chai, T., & Draxler, R. R. (2014). Root mean square error (RMSE) or mean absolute error (MAE)?—Arguments against avoiding RMSE in the literature. *Geoscientific model development*, 7(3), 1247-1250.

[39] Rogers, D. J., & Tanimoto, T. T. (1960). A computer program for classifying plants. *Science*, 132(3434), 1115-1118.

[40] Wang, Z., Simoncelli, E. P., & Bovik, A. C. (2003, November). Multiscale structural similarity for image quality assessment. In *The Thirty-Seventh Asilomar Conference on Signals, Systems & Computers, 2003* (Vol. 2, pp. 1398-1402). Ieee.

[41] Otsu, N. (1979). A threshold selection method from gray-level histograms. *IEEE transactions on systems, man, and cybernetics*, 9(1), 62-66.

[42] Gulli, A., & Pal, S. (2017). *Deep learning with Keras*. Packt Publishing Ltd.

[43] Tan, M., & Le, Q. (2019, May). Efficientnet: Rethinking model scaling for convolutional neural networks. In *International Conference on Machine Learning* (pp. 6105-6114). PMLR.

[44] Paszke, A., Chaurasia, A., Kim, S., & Culurciello, E. (2016). Enet: A deep neural network architecture for real-time semantic segmentation. *arXiv preprint arXiv:1606.02147*.

[45] Minaee, S., Boykov, Y. Y., Porikli, F., Plaza, A. J., Kehtarnavaz, N., & Terzopoulos, D. (2021). Image segmentation using deep learning: A survey. *IEEE Transactions on Pattern Analysis and Machine Intelligence*.

[46] Ma D., Wu H., Sun J., Yu C., Liu L. (2019) A Light-Weight Context-Aware Self-Attention Model for Skin Lesion Segmentation. In: Nayak A., Sharma A. (eds) *PRICAI 2019: Trends in Artificial Intelligence*. PRICAI 2019. Lecture Notes in Computer Science, vol 11672. Springer, Cham.

[47] Zhang, J., Xie, Y., Zhang, P., Chen, H., Xia, Y., & Shen, C. (2019, August). Light-Weight Hybrid Convolutional Network for Liver Tumor Segmentation. In *IJCAI* (pp. 4271-4277).

[48] Ding, M., & Fenster, A. (2003). A real-time biopsy needle segmentation technique using Hough Transform. *Medical physics*, 30(8), 2222-2233.

[49] Dillinger, P., Vogelbruch, J. F., Leinen, J., Suslov, S., Patzak, R., Winkler, H., & Schwan, K. (2005, June). FPGA based real-time image segmentation for medical systems and data processing. In *14th IEEE-NPSS Real Time Conference, 2005*. (pp. 5-pp). IEEE.

[50] Ouahabi, A., & Taleb-Ahmed, A. (2021). Deep learning for real-time semantic segmentation: Application in ultrasound imaging. *Pattern Recognition Letters*, 144, 27-34.

[51] Chen, L. C., Zhu, Y., Papandreou, G., Schroff, F., & Adam, H. (2018). Encoder-decoder with atrous separable convolution for semantic image segmentation. In *Proceedings of the European conference on computer vision (ECCV)* (pp. 801-818).

[52] Chen, L. C., Papandreou, G., Schroff, F., & Adam, H. (2017). Rethinking atrous convolution for semantic image segmentation. *arXiv preprint arXiv:1706.05587*.

## Appendix

Table 8. Average segmentation accuracy for each sample. Bold value is the maximum for each participant. “P” is patient and “V” is volunteer.

	P1	P2	P3	P4	P5	P6	P7	P8	P9	P10	P11	P12	P13	P14	P15	V1
U-Net*	84.5	86.4	86.8	92.7	88.2	89.8	88.9	79.1	87.6	93.5	84.8	89.5	92.5	86.1	92.3	92.3
U-Net	85.2	87.9	87.0	94.4	89.1	91.1	89.7	79.8	89.4	94.0	87.0	90.1	93.3	87.7	93.1	93.1
Inception v3	89.8	93.5	88.7	95.2	91.1	93.4	90.4	85.8	94.3	96.1	93.2	95.1	96.4	93.0	95.5	95.5
MultiResUNet	88.2	92.9	90.5	96.7	91.8	90.5	89.0	89.6	90.5	95.3	84.0	91.1	95.2	87.0	95.9	95.9
EfficientNet b0	89.0	93.6	90.1	95.7	90.4	93.7	89.1	84.3	94.3	94.5	92.6	96.2	95.9	89.0	95.5	95.5
DC-UNet	<b>90.3</b>	<b>94.7</b>	91.1	<b>96.7</b>	<b>90.7</b>	92.4	90.0	83.4	91.4	95.5	92.6	95.9	97.6	90.1	95.7	95.7
MobileNetv2	89.0	93.2	91.1	94.8	90.2	93.2	90.3	83.3	93.9	94.9	90.3	93.8	94.2	90.1	94.8	94.8
ICNet	86.7	82.3	84.3	85.3	86.4	87.2	81.7	82.0	87.4	84.3	80.1	84.4	85.1	88.3	85.9	85.9
ESPNNet	87.9	80.0	89.8	91.7	86.3	90.5	88.5	75.2	87.8	86.8	89.2	93.3	91.5	88.3	<b>96.9</b>	96.9
ENet	82.3	85.7	88.8	89.7	87.9	85.3	85.9	78.3	89.6	83.5	73.2	85.9	82.7	73.4	87.7	87.7
CFPNet-M	87.5	89.7	<b>93.0</b>	93.8	90.4	92.0	90.2	<b>88.2</b>	91.7	93.9	93.5	95.5	93.6	93.4	96.0	96.0
	V2	V3	V4	V5	V6	V7	V8	V9	V10	V11	V12	V13	V14	V15	V16	
U-Net*	91.4	89.5	91.0	87.8	84.1	91.7	82.6	93.8	82.5	92.7	93.3	88.2	90.4	92.3	87.2	87.2
U-Net	92.2	90.4	92.7	88.7	85.5	92.5	84.3	94.3	95.6	90.1	<b>97.3</b>	<b>96.5</b>	<b>93.7</b>	91.8	87.9	87.9
Inception v3	<b>95.4</b>	91.9	<b>94.5</b>	<b>93.6</b>	91.0	94.3	87.6	95.6	88.4	96.5	95.7	89.6	93.2	95.3	<b>95.2</b>	<b>95.2</b>
MultiResUNet	93.0	90.8	92.6	90.3	90.1	93.9	88.2	96.0	90.3	96.5	95.0	95.0	92.5	95.2	89.0	89.0
EfficientNet b0	94.8	91.4	93.5	92.7	<b>93.0</b>	93.2	<b>90.3</b>	95.9	90.3	96.5	97.1	95.5	93.0	94.1	94.2	94.2
DC-UNet	93.8	<b>93.6</b>	94.1	91.4	95.4	88.4	<b>96.9</b>	89.3	97.1	96.5	90.4	96.0	93.1	91.8	91.0	91.0
MobileNetv2	91.7	91.1	92.8	92.0	91.7	91.6	87.2	95.0	90.4	89.6	86.3	82.2	84.3	94.2	94.8	94.8
ICNet	85.9	81.9	86.7	81.2	85.0	87.7	87.0	82.5	89.8	84.5	86.4	82.2	93.1	84.7	85.1	85.1
ESPNNet	89.8	92.4	89.1	92.8	94.9	85.7	94.5	94.8	79.0	87.7	87.3	86.9	92.6	93.9	93.1	93.1
ENet	84.7	86.9	88.3	85.4	89.4	93.7	81.2	94.8	94.3	88.9	90.8	95.2	96.1	91.8	91.5	89.6
CFPNet-M	89.4	91.6	90.4	93.0	90.9	94.3	88.9	94.8	94.3	90.9	94.8	95.2	96.1	<b>95.8</b>	91.2	91.2